Nanoscale

Check for updates

Phase diagram and structural evolution of tin/indium (Sn/In) nanosolder particles: from a non-equilibrium state to an equilibrium state†

Yang Shu,[a] Teiichi Ando,[b] Qiyue Yin,[c] Guangwen Zhou [iD][c] and Zhiyong Gu [iD] *[a]

A binary system of tin/indium (Sn/In) in the form of nanoparticles was investigated for phase transitions and structural evolution at different temperatures and compositions. The Sn/In nanosolder particles in the composition range of 24–72 wt% In were synthesized by a surfactant-assisted chemical reduction method under ambient conditions. The morphology and microstructure of the as-synthesized nanoparticles were analyzed by scanning electron microscopy (SEM), high resolution transmission electron microscopy (HRTEM), selected area electron diffraction (SAED) and X-ray diffraction (XRD). HRTEM and SAED identified $InSn_4$ and In, with some Sn being detected by XRD, but no In_3Sn was observed. The differential scanning calorimetry (DSC) thermographs of the as-synthesized nanoparticles exhibited an endothermic peak at around 116 °C, which is indicative of the metastable eutectic melting of $InSn_4$ and In. When the nanosolders were subjected to heat treatment at 50–225 °C, the equilibrium phase In_3Sn appeared while Sn disappeared. The equilibrium state was effectively attained at 225 °C. A Tammann plot of the DSC data of the as-synthesized nanoparticles indicated that the metastable eutectic composition is about 62% In, while that of the DSC data of the 225 °C heat-treated nanoparticles yielded a eutectic composition of 54% In, which confirmed the attainment of the equilibrium state at 225 °C. The phase boundaries estimated from the DSC data of heat-treated Sn/In nanosolder particles matched well with those in the established Sn–In equilibrium phase diagram. The phase transition behavior of Sn/In nanosolders leads to a new understanding of binary alloy particles at the nanoscale, and provides important information for their low temperature soldering processing and applications.

1. Introduction

In recent years, due to the health risk and environmental problems of lead (Pb) containing soldering materials, many studies have been carried out in order to seek for alternative solders.[1,2] Most current lead-free solder materials tend to have higher melting temperatures, weaker mechanical properties, and higher occurrence of undesirable intermetallic compounds than the traditional tin–lead (Sn/Pb) solders.[3–6] Furthermore, with the miniaturization of consumer electronics and devices, solder materials are required to be stronger, as

well as be able to connect smaller components together while having lower processing temperatures.[3–7] This is especially true for the assembly and packaging of flexible electronics[8] and heat sensitive components such as LEDs, which require low assembly temperatures and small-scale joining.

Nanosolders stood out among the candidates to replace the traditional Sn/Pb solders because some currently used lead-free solders have relatively high melting temperatures; the low melting temperature of the nanosolders and the ability to join small features make them ideal for micro/nanoscale assembly and soldering applications.[9–11] Several nanosolder systems have been developed, such as Sn–Ag–Cu (SAC),[12–16] Sn–Ag,[17–21] Ni–Sb–Sn,[22] Sn–Bi,[23–25] and Sn–In.[26–28] Joining applications using the nanosolders are currently being developed.[13,15,18,19,26,27] It is also found that solders with the addition of nanoparticles tend to have a smaller grain size[11,29–32] and significantly slower intermetallic compound (IMC) growth during the aging[33–37] that improved the mechanical properties.

However, the understanding of the thermal properties of nanosolders, such as melting temperature and phase behavior, has been very limited, especially for binary or ternary alloys.

[a]Department of Chemical Engineering, University of Massachusetts Lowell,
One University Ave, Lowell, MA 01854, USA. E-mail: Zhiyong_Gu@uml.edu
[b]Department of Mechanical and Industrial Engineering, Northeastern University,
360 Huntington Ave, Boston, MA 02115, USA
[c]Department of Mechanical Engineering & Multidisciplinary Program in Materials
Science and Engineering, State University of New York, Binghamton,
4400 Vestal Parkway East, Binghamton, NY 13902, USA
†Electronic supplementary information (ESI) available. See DOI: 10.1039/
c7nr01402c

Their phase diagrams and phase transitions will improve the understanding of nanosolders which can provide important information for their composition selection, solderability and ultimately joint quality. Thermodynamic approaches of nanosolder phase diagrams using Computer Calculation of Phase Diagram (CALPHAD) modeling have been explored, including Sn–Ag[38] and SAC systems.[39] While providing some valuable information, the theoretical approach is still limited in scope.

Tin/indium (Sn/In) solder alloys, with a eutectic temperature of 118 °C at Sn/In 48/52, are useful as low temperature solders for assembling electronics and devices that are susceptible to temperature damage if conventional solders are used, and for their excellent properties of ductility and malleability. Sn/In solders also wet glass, quartz, and ceramic materials, which makes them suitable for metal to non-metal joining. In addition, Sn/In is a binary system with two intermetallic compounds γ-InSn$_4$ and β-In$_3$Sn in a wide composition range, making it an ideal system to investigate the nanoscale phase diagram and phase transition.[40] From the previous study on the synthesis and characterization of Sn/In nanosolder particles,[26] a wide composition range (24% to 72% In) of Sn/In nanosolder particles has been achieved. In the present study, the phase transition of Sn/In nanosolder particles has been investigated under different temperature treatments. HRTEM, XRD and DSC were used to investigate their structural transition along different temperatures and compositions. Tammann diagrams were used to obtain the eutectic composition. Finally, phase transition from the as-synthesized nanoparticles (non-equilibrium state) to heat-treated samples (equilibrium state) was discussed.

2.   Experimental

2.1   Materials and chemicals used

Sodium dodecyl sulfate (SDS) (85%) and ethanol (anhydrous) were purchased from Fisher Scientific. Tin sulfate (SnSO$_4$, 99%), indium chloride (InCl$_3$, 99.995%) and sodium borohydride (NaBH$_4$, 99%) were purchased from Acros Organics. Hydrochloric acid (HCl, 36.5%–38%) was obtained from VWR Scientific. DI water was obtained from a Barnstead Nanopure water purification system. All materials were used without further purification.

2.2   Sn/In nanosolder particle synthesis and heat treatment

Sn/In nanosolder particles were synthesized by a surfactant assisted chemical reduction method.[26] Specimens with different starting mass ratios of Sn/In 80/20, 70/30, 60/40, 50/50, 40/60, and 30/70 were synthesized by varying the amounts of the Sn and In salts in the precursor solutions. First, SDS was dissolved in DI water to form an 8 mM solution. Then HCl was added to the solution to adjust the pH to about 2.7. Then the precursors of SnSO$_4$ and InCl$_3$ in the desired amounts were added to the solution. An excess amount of NaBH$_4$ was slowly added to the precursor solution with a syringe pump (single-syringe infusion pump, KDS LEGATO 110, KD

Scientific) at a constant speed of 25 mL h^{-1}. Then the solution was kept at room temperature for 30 minutes to allow for the formation of Sn/In nanoparticles. After the reaction was complete, the nanoparticles were separated from the solution by centrifugation using an Eppendorf 5804 centrifuge at 7000 rpm and washed 5 times with DI water and 3 times with ethanol through dispersion and centrifuge cycles.

After the washing step, the as-synthesized Sn/In nanosolder particles were dried in a vacuum oven (Vacuum Oven Model 29, Precision). The dried Sn/In nanoparticles were then heat treated at 50 °C, 100 °C, 125 °C, 150 °C, and 250 °C, respectively, for 3 h in a tube furnace (Lindberg/Blue M, Thermal Scientific) with nitrogen purging. The heat-treated samples were then immediately subjected to the XRD and DSC tests.

2.3   Characterization

Sn/In nanoparticles were examined by scanning electron microscopy (SEM, JEOL7401F field emission-SEM) for their morphology and size. The elemental composition of the Sn/In nanosolder particles with different Sn/In ratios was examined by using an energy dispersive X-ray spectrometer (EDS) equipped on the FE-SEM. Transmission electron microscopy (JEOL EM2100F) was also used to examine the morphology of the nanosolder particles as well as to identify the crystal structure of individual nanoparticles. The Sn/In nanoparticles, with and without heat treatment, were subjected to X-ray diffraction (XRD, BRUKER AXS D5005 X-ray diffractometer, Cu KR radiation, λ = 1.540598 Å) to identify the phases present in the specimens. Differential scanning calorimetry (DSC, TA Instruments Q100) was used to determine the phase transition temperatures of the specimens, at a heating rate of 10 °C min^{-1} from 50 °C to 300 °C.

3.   Results and discussion

3.1   As-synthesized Sn/In nanosolder particles

Nanosolder particles with starting Sn/In ratios of 80/20, 70/30, 60/40, 50/50, 40/60, and 30/70 were obtained through the surfactant-assisted chemical reduction method. The specimens below 20% In and above 70% In were also synthesized; however, it was observed that the nanoparticles were either not uniform (such as larger particles >100 nm or other shaped nanoparticles) or had a lot of hydrolysis and thus the yield and quality of Sn/In nanoparticles were low. Therefore, only the nanoparticles with the starting indium content from 20% to 70% were used in the following experiments. Fig. 1 shows the SEM images and size analyses of the as-synthesized Sn/In nanosolder particles with the Sn/In elemental ratios of 70/30, 50/50, and 30/70, respectively. The particles in the Sn/In 70/30 specimen are mostly within the size range of 40 to 70 nm; the size range of nanoparticles in the Sn/In 50/50 specimen is mostly 40 to 80 nm, which compares well with the results from the TEM imaging (Fig. S-1†). For the Sn/In 30/70 specimen, the nanoparticles are mostly in the range of 40 to 90 nm. The nanoparticles tend to have a larger size as the indium content
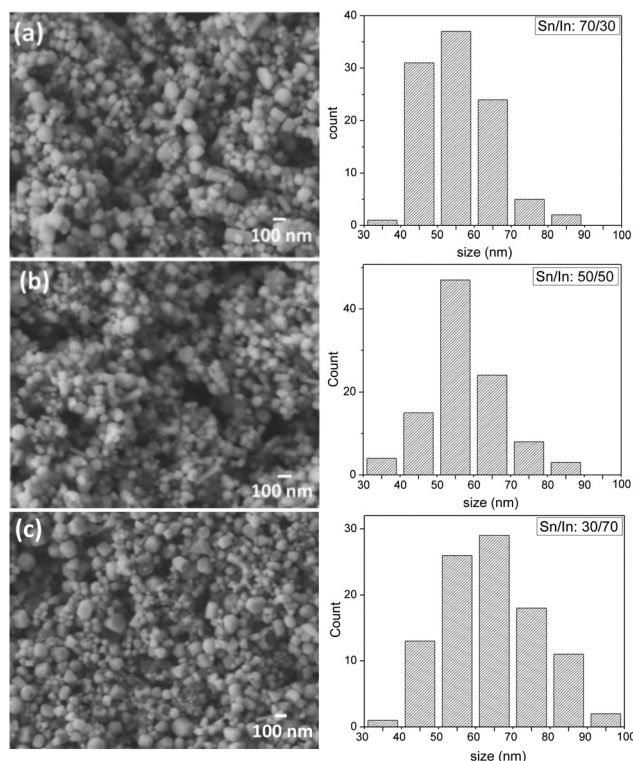
Fig. 1 SEM images and the size analysis of Sn/In nanosolder particles at Sn/In compositions: (a) 70/30, (b) 50/50, and (c) 30/70.

Fig. 2 EDS results of Sn/In nanoparticles at different weight compositions.

increases. The actual compositions of each Sn/In specimen were characterized by EDS, which was taken as the average of at least three different spots in each specimen. From the EDS results, about 4 wt% of oxygen (O) was found in the as-synthesized Sn/In nanosolder particles at all Sn/In compositions investigated, which was from the oxide on the surface of the nanoparticles. The EDS results of the Sn/In specimens are plotted against the starting precursor composition (Fig. 2). It is seen that the In contents in the as-synthesized nanosolder particles are slightly higher than the starting In contents, which might contribute to larger nanoparticle sizes as the In content increased.

3.2 Structure analysis of the as-synthesized Sn/In nanosolder particles

XRD was used to identify the phases at different Sn/In compositions (Fig. S-2†).[26] From the XRD results, at 24% In, mainly $InSn_4$ peaks with small Sn peaks were observed. In the XRD spectra of other Sn/In compositions (35%–72%), both $InSn_4$ and In can be observed. The intensity of In peaks increased from almost negligible (less than 10% intensity) at 35% In to the highest peak at 72% In, whereas the $InSn_4$ decreased accordingly in the same range of In concentration. The absence of the equilibrium phase In_3Sn at the compositions studied indicates that the as-synthesized Sn/In nanosolder particles were in a non-equilibrium state. The specimens were also characterized by DSC to investigate the thermal properties
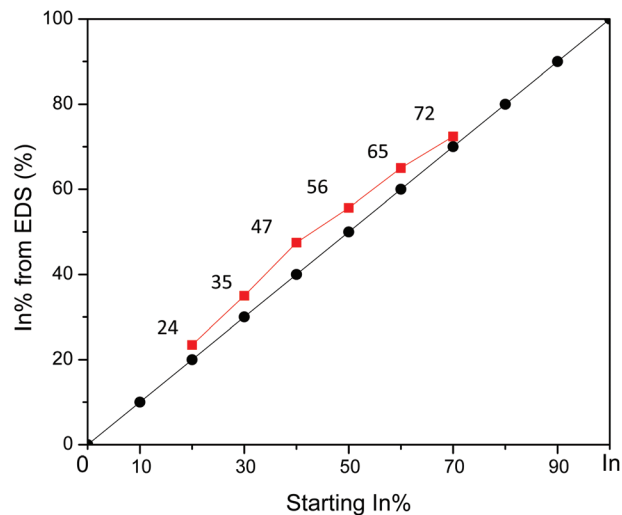
of the six specimens with different Sn/In compositions (Fig. S-3†).[26] An endothermic peak at 223.5 °C and a minor peak on the left (115.6 °C) were observed on the DSC curve of the 24% In sample; comparing with the XRD results shown in Fig. S-2,† the peak at 223.5 °C indicates the melting of Sn nanoparticles, while the small peak at 115.6 °C suggests the metastable eutectic melting between $InSn_4$ and In (though the presence of In may be in a small amount not detectable by XRD). For the 35% In specimen, there was one major peak observed around 115.5 °C, indicating that the metastable eutectic melting was the dominant event in this composition with the 35% In specimen. For the specimen of 47% to 72% In, a small peak on the right of the main peak around 116–118 °C can be observed, suggesting that the specimens underwent metastable eutectic melting at 116–118 °C, then followed by the melting of the remaining In at the liquidus temperature at 122.8 °C, 125 °C, 128.7 °C, and 148.4 °C, respectively.

Comparing the above phase behavior with the equilibrium Sn/In phase diagram,[40] significant differences can be observed. At the equilibrium state, the 24% In specimen is expected to consist mainly of $InSn_4$ at room temperature,[40] but the phases present in the as-synthesized nanoparticles are $InSn_4$ and Sn. Also, the eutectic composition of the Sn–In system at the equilibrium state was reported to be 52% In with the contribution from $InSn_4$ and In_3Sn. However, in the present study the In_3Sn phase was absent in the Sn/In nanosolder particles at any of the compositions examined. Instead, In was found from the specimens with the indium content from 35% to 72%, whereas In should only be observed from 88% to 100% In if the alloy is at the equilibrium state. The absence of the In_3Sn phase and the phase boundary shift suggested that the as-synthesized Sn/In nanosolder particles were not in the equilibrium state. Therefore, a series of heat treatments were conducted to investigate the phase transition of the Sn/In nanosolder particles.

3.3 HRTEM analysis of the as-synthesized Sn/In nanosolder particles

The morphology and crystal structures of the as-synthesized Sn/In nanosolder particles with different elemental compositions were also examined by HRTEM. Fig. 3a represents the morphology of a typical polyhedral nanoparticle that was found in the 35% In specimen. The HRTEM image of this particle is shown in Fig. 3b. Fig. 5c shows a calculated Fast Fourier Transform (FFT) pattern from the selected area marked by the white dashed square as indicated in Fig. 3b. The HRTEM image in Fig. 3b clearly reveals that the nanoparticle is a single crystal with a thin (<5 nm) layer of amorphous oxide on the surface. The interplanar spacing d measured from the HRTEM image is 0.28 nm, which is close to 0.278 nm for $InSn_4$ $\{10\bar{1}0\}$ or 0.279 nm for β-Sn $\{011\}$. The FFT diffraction pattern as shown in Fig. 5c can only be indexed as $InSn_4$ along the <0001> zone axis because $InSn_4$ is hexagonal ($P6/mmm$).

Therefore, the phase and structure of nanoparticles in the 35% In specimen are confirmed as $InSn_4$. TEM examination of other nanoparticles of this specimen further confirmed the crystallinity and phase of the nanoparticles in the 35% In specimen as single crystals of $InSn_4$. The analysis agreed with the XRD analysis shown. From the XRD result, a very small amount of In should also be present in this specimen (see Fig. S-2†); however, due to the limited number of nanoparticles that were examined by HRTEM, In nanoparticles were not found through HRTEM imaging.

The HRTEM analysis of the 56% In specimen is shown in Fig. 4. Two typical types of nanoparticles were found in this composition. Fig. 4a represents one typical structure of the nanoparticles. The inset in Fig. 4a is a low magnification bright field (BF)-TEM image of the nanoparticle, from which we can see the size and the shape of the particle. The diffraction pattern from the area marked by the dashed square in Fig. 4a is shown in Fig. 4b. It matches well with the diffraction pattern of In along the <100> zone axis. Fig. 4c represents another typical structure of the nanoparticles in the 56% In specimen. The HRTEM of Fig. 4c is taken from the edge of the particle indicated by the red arrow in the low magnification image in the inset. The diffractogram from the area marked by the white dashed square in Fig. 4c is shown in Fig. 4d, which matches well with $InSn_4$ along the [0001] zone axis. Therefore, the two typical phases of nanoparticles in the 56% In specimen are In and $InSn_4$, respectively. The results match well with the XRD observation in the previous section (Fig. S-2†), and further confirmed that a mixture of both In and $InSn_4$ phases exists in the form of separate single crystalline nanoparticles. The In particles are well rounded and the $InSn_4$ particles are faceted.

Similar to the 56% In specimen, two types of nanoparticles were found in the 72% In specimen. Fig. 5a shows a HRTEM
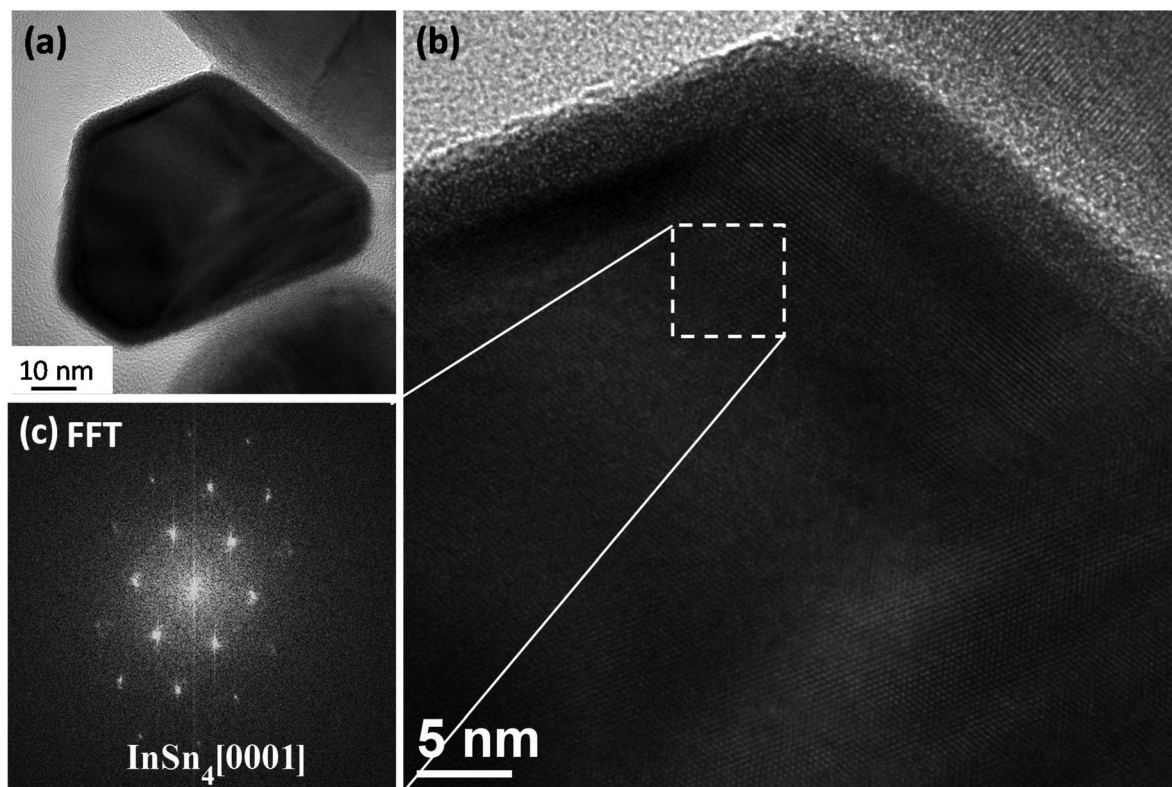

Fig. 3 (a) Morphology of the 35% In specimen, (b) HRTEM image of the particle as shown in (a), (c) diffractogram from the selected area marked by the white dashed square indicated in (b).
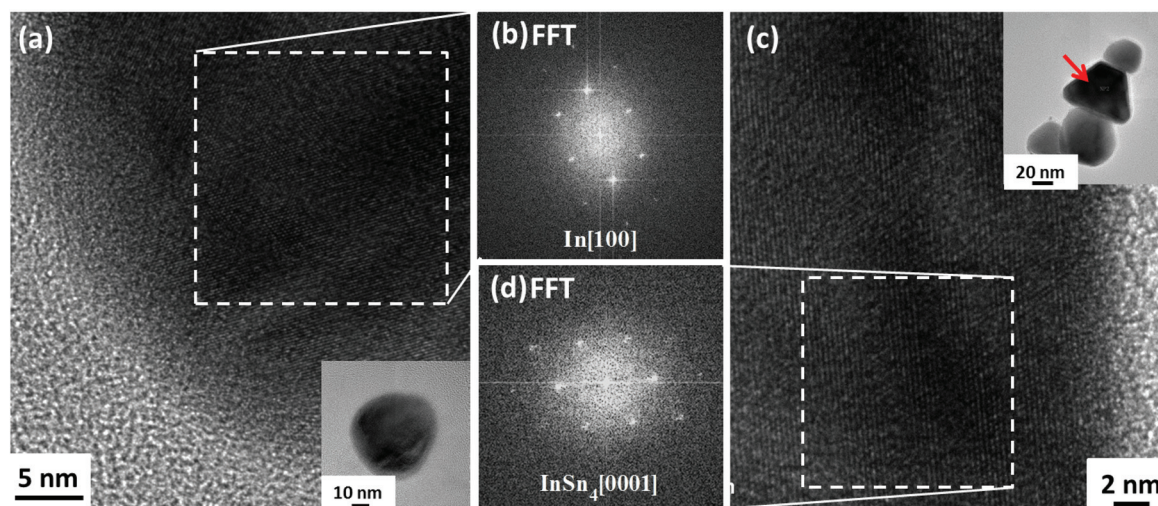
Fig. 4 56% In specimen, (a) HRTEM image and low-magnification TEM image (inset) of an In nanoparticle, (b) diffractogram from the area marked by the white dashed square in (a); (c) HRTEM image and low-magnification TEM image (inset) of an $InSn_4$ nanoparticle, (d) diffractogram from the area marked by the white dashed square in (c).
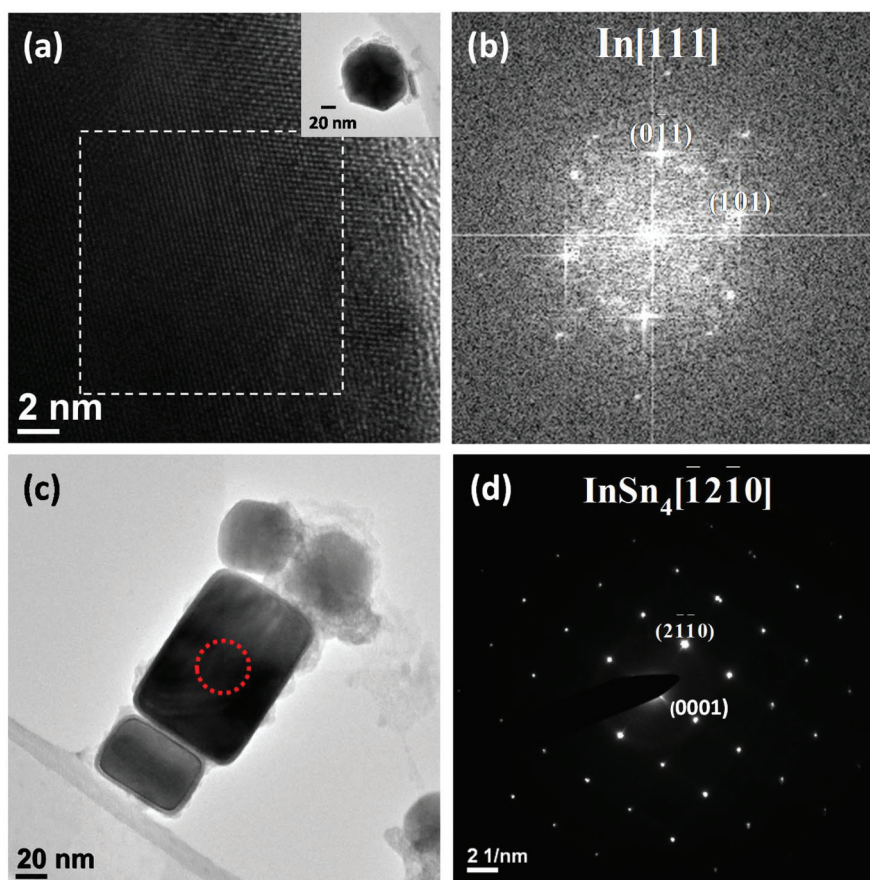

Fig. 5 72% In specimen; (a) HRTEM image and low magnification TEM image (inset) of an In particle, (b) diffractogram of the area marked by the white dashed square in (a); (c) BF-TEM image of $InSn_4$ nanoparticles, (d) electron diffraction pattern taken from the area encircled by the red dashed line in (c).

image and a low-magnification overview (inset) of one of the two types of the nanoparticles in the 72% In specimen. Fig. 5b is a FFT calculated pattern from the area marked by the dashed line in Fig. 5a, which matches well with that of In along the [111] zone axis. Another type of nanoparticle in the sample is shown in Fig. 5c. An electron diffraction pattern taken from the area encircled by the red dashed line in Fig. 5c is shown in Fig. 5d. The diffraction pattern is indexed and matches well with hexagonal $InSn_4$ along $[\bar{1}2\bar{1}0]$. Compared to the 56% In specimen, more In nanoparticles were found during the examination; however, the particles that were found in this composition are still In and $InSn_4$ nanoparticles, which agreed with the XRD analysis as well.

3.4 Heat-treated Sn/In nanosolder particles

From the analysis shown above, it is found that the as-synthesized Sn/In nanosolder particles are in a non-equilibrium state. Equilibrium states may be achieved if it is given sufficient time. But the time to achieve equilibrium may be so long (the kinetics is so slow) that a state not at an energy minimum may appear to be stable. Therefore, a series of heat treatment have been applied to the as-synthesized Sn/In nanosolder particles to accelerate the transition of Sn/In nanosolder particles from the as-synthesized non-equilibrium state to an equilibrium state.

Fig. 6 shows the DSC curves and XRD spectra of the as-synthesized 24% In specimen and the same samples that were heat treated at 50, 100, 125, 150, and 225 °C for 3 h, respectively. At room temperature, the as-synthesized nanosolder particles showed one major endothermic peak at 223.5 °C on the DSC curve, corresponding to the melting of Sn nanoparticles

as discussed on the basis of the XRD result. As the heat treatment temperature increased to 50 °C and continued to increase to 150 °C, the small peak at around 115.6 °C started to increase and ranged between 114.7 °C and 117.5 °C, which is slightly below the equilibrium eutectic temperature of the Sn/In at the equilibrium state, suggesting that the peak around these positions is contributed by the metastable eutectic melting between $InSn_4$ and In. As the heat treatment temperature increased to 225 °C, the major peak shifted from 223.5 °C to 201.3 °C, indicating that this temperature became closer to the equilibrium liquidus temperature of the Sn/In alloy at 24% In. It is also notable that in the specimen heated at 100 °C, 125 °C, and 150 °C, an exothermic peak around 220–250 °C can be observed, which is possibly from the crystallization of tin oxide (SnO_x).[13] While for the specimen heated to 225 °C, the heating temperature reached the crystallization temperature of SnO_x, and thus this exothermic peak was not observed in the DSC curve. The corresponding XRD spectra (Fig. 6b) showed that, while the $InSn_4$ peak remained to be the major peaks, the Sn peak became smaller as the treatment temperature increased. Also, for the specimens treated at 100–150 °C, a small In peak emerged. These results indicate that the heat treatment temperature from 50–150 °C is not sufficient to reach the equilibrium state. For the specimen after 225 °C treatment, the Sn peak became very small, indicating that a small amount of isolated Sn particles still remained. In the meanwhile, a small peak at 50.9° corresponding to the SnO crystal showed up in the XRD spectrum of the specimen. It is confirmed that the amorphous SnO crystallized during the 225 °C treatment, and the exothermic peak observed on the DSC curves of the 50–150 °C treatments was from the crystalli-
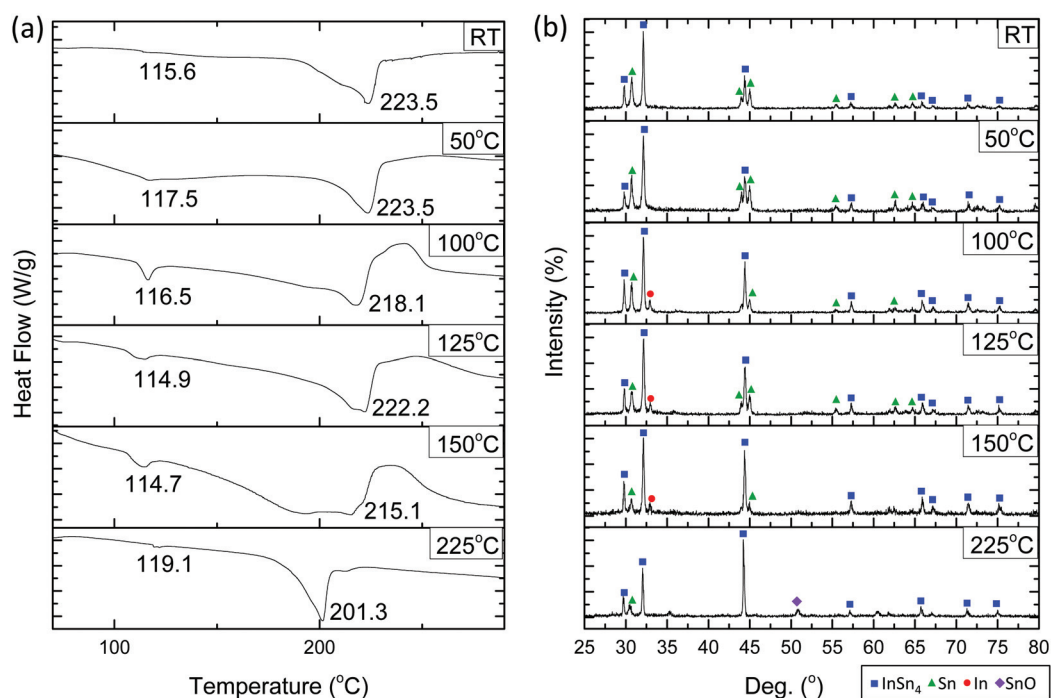

Fig. 6 Specimen of 24% In treated at different temperatures: (a) DSC curves and (b) XRD spectra.

zation of SnO. From the XRD of the 225 °C specimen, it can be observed that the major compound that was present after the 225 °C heat treatment was $InSn_4$, which is very close to the result of the equilibrium phase diagram at 24% In.[40] As the temperature increased to 225 °C, the Sn/In nanosolder particles with 24% In moved from the metastable state to the equilibrium state.

The comparison of the 35% In specimen heated at different temperatures is shown in Fig. 7. From the DSC curve (Fig. 7a), the as-synthesized Sn/In nanosolder particles only showed one peak at 115.5 °C, whereas as the heat treatment temperature was increased, another peak at around 205 °C appeared. This peak remained relatively unchanged in the heat treatment temperature range from 50 °C to 150 °C; however, it shifted to 175.1 °C after the specimen was heat treated at 225 °C, which is close to the liquidus point at 35% In at the equilibrium state. In the heat treatment temperature range from room temperature to 150 °C, the peak around 115.5 °C remained relatively the same, indicating metastable eutectic melting in these samples; however, when the heat treatment temperature was increased to 225 °C, the peak temperature increased to 119.7 °C, close to the equilibrium eutectic temperature. Also, the corresponding XRD spectra (Fig. 7b) show only $InSn_4$ in the as-synthesized sample, but $InSn_4$, Sn, and In in the samples heat treated up to 150 °C. When the heat treatment temperature was increased to 225 °C, the specimen consisted mainly of $InSn_4$ and Sn, with new peaks emerging as In_3Sn. These results indicate that when the treatment temperature

was increased to 225 °C, the 35% In specimen effectively reached the equilibrium state (with a small amount of isolated Sn left). Also, a small peak of SnO at 50.9° can be observed from the spectra at 225 °C, similar to the observation at 24% In composition.

56% is the In content that is the closest to the equilibrium eutectic composition of Sn/In 48/52. A series of DSC curves and XRD spectra are shown in Fig. 8. In the DSC curves, when the heat treatment temperature increased to 50 °C, the metastable eutectic melting peak at 116.1 °C shifted to 119.7 °C, close to the equilibrium eutectic melting temperature. A similar trend was observed for the treatment temperatures from 100 to 150 °C. The shoulder peak on the right of the main peak in the as-synthesized specimen, as the treatment temperature was increased to 150 °C, moved to a larger peak and higher temperature in the range of 123.3 to 127.5 °C. Then the two peaks merged into one peak at 121.1 °C after the 225 °C treatment, which indicated that the composition became close to the equilibrium eutectic composition. Similar to the 24% In specimen, an exothermic peak of SnO crystallization was observed for the specimens treated at temperatures below 225 °C (50–150 °C). At room temperature, both XRD and HRTEM confirmed that the 56% In specimen consisted of $InSn_4$ and In nanoparticles. In the XRD spectra of the specimens that were heat treated between 50 and 225 °C, peaks located at 32.92°, 36.52°, 41.36°, 53°, 56.4°, 63.36°, and 69.14° revealed that these peaks are for the In_3Sn phase. And the In_3Sn peaks grew taller as the treatment temperature increased.
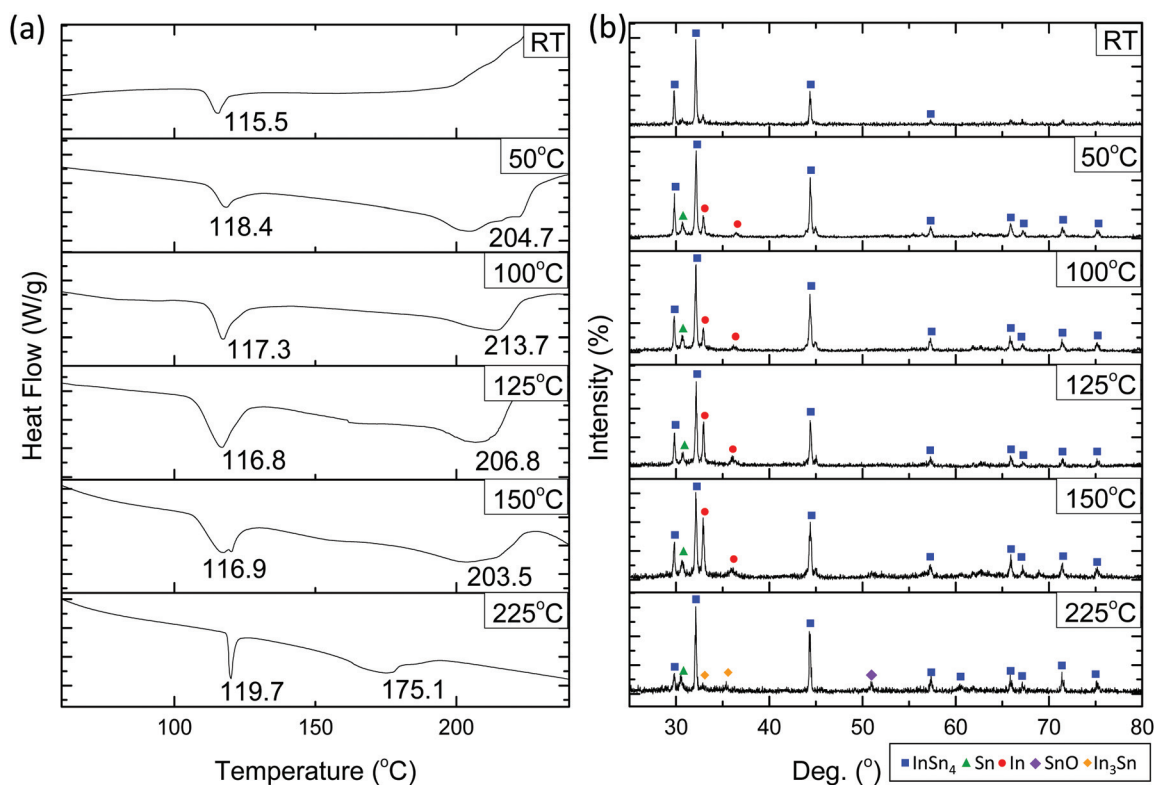

Fig. 7   35% In specimen treated at different temperatures: (a) DSC curves and (b) XRD spectra.
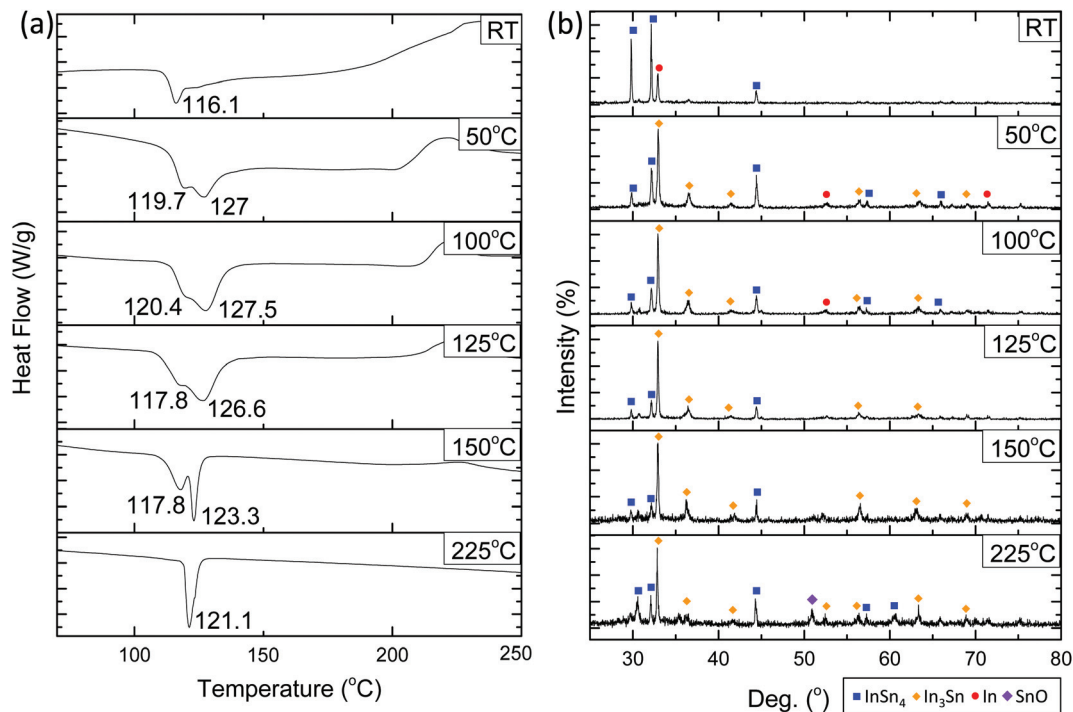
Fig. 8 Specimen of 56% In treated at different temperatures: (a) DSC curves and (b) XRD spectra.

The In_3Sn phase in the equilibrium phase diagram was reported to be in the range of 56% to 88% In, and the left boundary of the In_3Sn phase moved towards the Sn rich side as the temperature increases.[40] Based on the lever rule, it indicated that as the temperature increases, the ratio of In_3Sn will increase at the composition of 56% In. In the equilibrium phase diagram of Sn/In, the In_3Sn phase concentration of the 56% In specimen also increased as the temperature increased. Compared to the specimens at 24% and 35% In, low temperature treatment has a more significant effect in facilitating the 56% In specimen moving from the initial non-equilibrium state to the equilibrium state as the heat treatment was applied.

The 72% In content is the composition with the most In in the composition range studied in this work. Before heating, a major metastable eutectic melting peak at 117.9 °C and a minor liquidus peak at 148.4 °C were shown in the specimen (see Fig. 9). At the heat treatment temperatures of 50 °C, 100 °C and 125 °C, multiple peaks were observed. The peak at 118–119 °C was caused by eutectic melting, whereas other two peaks, at around 140 °C and 152 °C were caused by the melting of In. When the heat treatment temperature was increased to 150 °C, the eutectic peak at 118 °C disappeared. Instead, only two peaks at 132.5 °C and 135.3 °C were observed, indicating a solidus at 132.5 °C and a liquidus at 135.3 °C. When the heating temperature increased to 225 °C, the two peak temperatures became 128.3 °C and 131.7 °C.

The above interpretation can be further confirmed by the corresponding XRD results which showed that, before heating, $InSn_4$ and In were the main phases present in the Sn/In nano-

solder particles, which should contribute to the metastable eutectic melting at 118 °C. When the heat treatment temperature was increased to 50 °C, 100 °C and 125 °C, three phases, $InSn_4$, In_3Sn, and In, were all existing in the specimens, contributing to the three endothermic peaks that were observed in the DSC curves as mentioned above: the metastable and equilibrium eutectic melting that produced the peak at 118–119 °C, and the incongruent melting of In_3Sn and In. The presence of the three phases is against the phase rule of a binary phase diagram, indicating that the specimen had not integrated into a united system. When the heat treatment reached 150 °C, the XRD peaks indicated that the main crystal structure that was present was In_3Sn. At the same time, the $InSn_4$ peaks became very small, indicating that the main compound that was present in the 72% In specimen was In_3Sn. From the previous discussion in section 3.2, 72% In is not within the composition range in the equilibrium state that eutectic melting would occur. Instead, the melting should follow the solidus at around 130 °C and the liquidus at around 132 °C, and the corresponding crystal structure will be In_3Sn. It can be observed that the specimen treated at 225 °C followed the phase transition behavior of the equilibrium Sn/In phase diagram. The three endothermic peaks that were observed in the DSC at 50 °C, 100 °C, and 125 °C transformed into two.

3.5 Eutectic point analysis

To construct the phase diagram of the Sn/In nanosolder particles based on the above observation of phase identification and phase transition temperatures, the eutectic composition needs to be determined. Proper determination of the eutectic
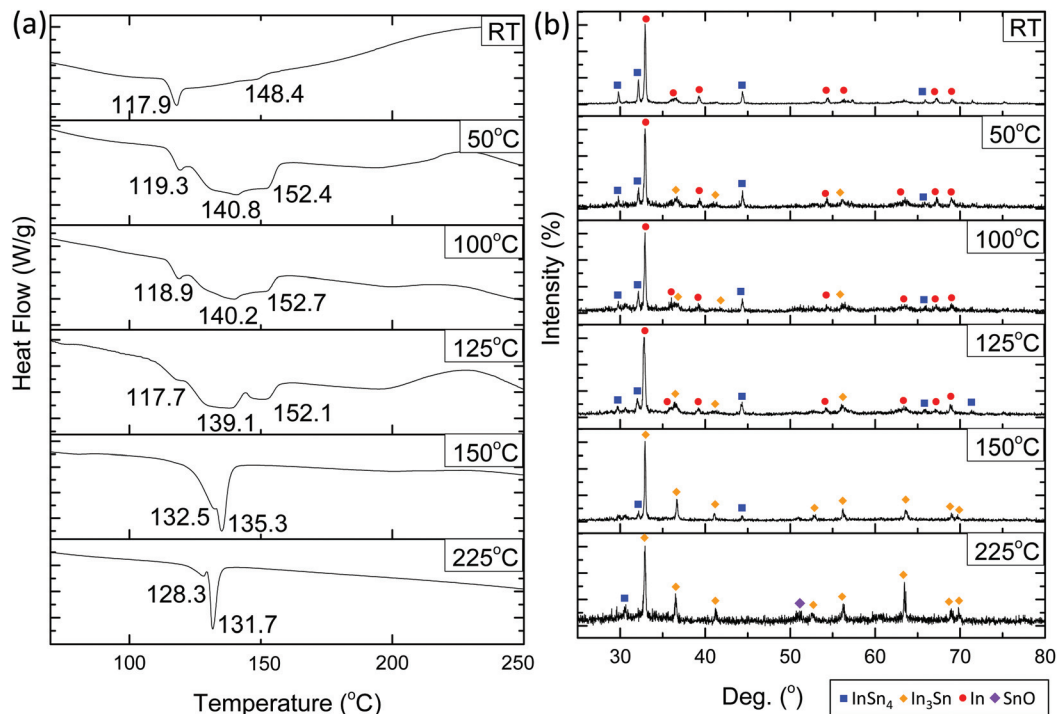
Fig. 9 Specimen of 72% In treated at different temperatures: (a) DSC curves and (b) XRD spectra.

point requires the creation of a Tammann diagram.[41] The Tammann diagram was plotted based on the lever rule of the phase diagram, and the size of the integrated eutectic signal (ΔH) should descend linearly depending on the fraction on both sides of the eutectic point. In this study, the first peak in the DSC plot was attributed to the eutectic melting. In some of the DSC curves, it is noticeable that there was overlapping of the thermal effect related to the eutectic melting and liquidus, especially at the compositions around 56% In. In order to correctly calculate the enthalpy related to eutectic, it is necessary to separate the overlapping peaks. The separation was made through TA Universal Analysis as well as calculating the enthalpy of the eutectic melting peak. Fig. 10 shows the Tammann diagram of the as-synthesized Sn/In nanosolder particles and the nanoparticles heat treated at 225 °C. The eutectic range of the nanoparticles changed from 32.7%– 75.2% In (as-synthesized) to 24.7%–65.4% In (after 225 °C treatment); and the eutectic composition shifted from 62.1% to 53.8%. Comparing the equilibrium Sn/In phase diagram, the eutectic range was reported to be 23%–57% In,[40] and the eutectic composition was observed to be 52% In. The eutectic point of the heat-treated Sn/In nanosolder particles is much closer to the reported eutectic point, and the eutectic range of the heated specimen is closer to the reported value as well. Thus, it is confirmed that the heat treatment facilitated the transformation of the as-synthesized Sn/In nanosolder particles from the initial non-equilibrium state to the equilibrium state. The heat treatment effectively accelerated the attainment of the equilibrium state.
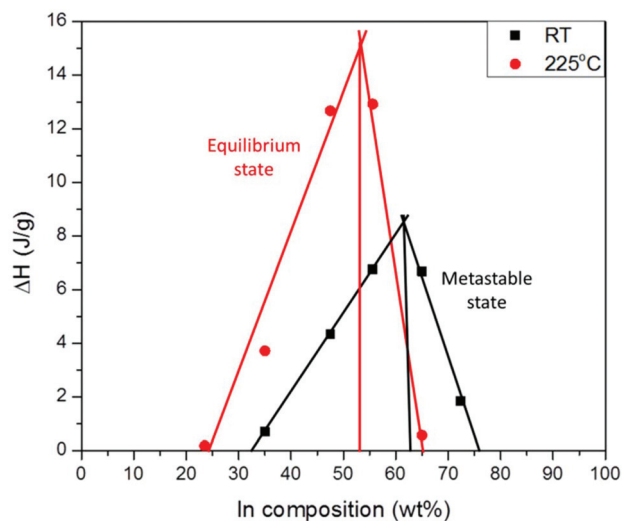

Fig. 10 Tammann diagram of the as-synthesized Sn/In nanosolder particles and the nanoparticles heat treated at 225 °C.

3.6 Phase diagram analysis

The eutectic composition and eutectic range were calculated from the respective Tammann diagrams. The eutectic range of the as-synthesized nanoparticles is 32.7%–75.2% In, and after 225 °C treatment the eutectic range is 24.7%–65.4% In. The eutectic compositions determined from the DSC data of the respective conditions are 62.1% and 53.8%. The above information may be used to construct full range phase diagrams.
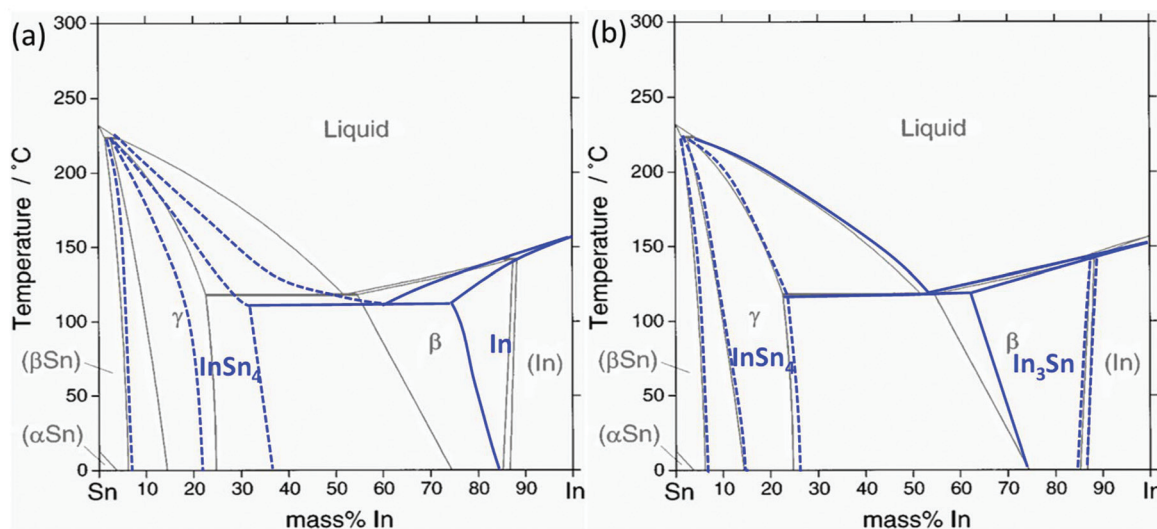
Fig. 11 Full range metastable phase diagram comparing with the equilibrium phase diagram: (a) the as-synthesized Sn/In nanosolder particles and (b) the nanoparticles heat treated at 225 °C.

Fig. 11 shows the metastable phase diagram of the as-synthesized Sn/In nanosolder particles and the equilibrium phase diagram of the 225 °C heat-treated nanoparticles. From Fig. 11a, the metastable phase boundaries, as well as the eutectic composition, of the as-synthesized Sn/In nanosolder phase diagrams are shifted to the In rich side. The metastable eutectic temperature is also observed to be slightly lower than the equilibrium eutectic point. In_3Sn is not observed from any of the compositions in the as-synthesized nanoparticles. However, after the heat treatment at 225 °C, the phase diagram of the Sn/In nanoparticles became nearly identical to the equilibrium phase diagram (see Fig. 11b), in which the In_3Sn phase occurs at 35% In and above specimens, and the In phase is no longer observed within the composition ranges. Heat treatments effectively accelerate the nanoparticle transformation from the non-equilibrium state to the equilibrium state.

4.   Conclusions

Sn/In nanosolder particles were synthesized by chemical reduction at Sn/In starting mass ratios of 80/20, 70/30, 60/40, 50/50, 60/40, and 70/30. The size of the nanoparticles is slightly dependent on their compositions and is mostly in the range of 40–90 nm, and the nanoparticles are covered with a thin overlayer of amorphous SnO. The as-synthesized specimens of 35% to 72% In consisted of single crystal nanoparticles of $InSn_4$ and In. Therefore, the Sn/In nanosolders are in a non-equilibrium state where In_3Sn was absent. As the heat treatment temperature was increased, the Sn/In nanosolder particles shifted toward the equilibrium state. The formation of In_3Sn is accelerated with the heat treatment. The eutectic composition moved from 62.1% to 53.8% In as the heat was applied. In the as-synthesized specimen, metastable eutectic melting between $InSn_4$ and In occurs in a composition range

between 32.7% and 75.2% In, which is much wider than that for the equilibrium eutectic melting between $InSn_4$ and In_3Sn (23–57% In). The phase transition phenomenon of the Sn/In nanosolder particles not only provides structure–property information of Sn/In solders at a nanoscale, but also contributes to the design and development of nanosolders for their potential application in a smaller scale.

Conflicts of interest

There are no conflicts of interest to declare.

Acknowledgements

References

1 *Electronics Manufacturing: With Lead-free, Halogen-Free, and Conductive-Adhesive Materials*, ed. J. Lau, C. P. Wong, N. C. Lee and S. W. R. Lee, McGraw Hill, New York, 2002.
2 Y. I. Li, K. Moon and C. P. Wong, *Science*, 2005, **308**, 1419–1420.
3 K. Zeng and K. N. Tu, *Mater. Sci. Eng., R*, 2002, **38**, 55–105.
4 D. A. Shnawah, M. F. Mohd Sabri and I. A. Badruddin, *Microelectron. Reliab.*, 2012, **52**, 90–99.

5 K. Suganuma, *Curr. Opin. Solid State Mater. Sci.*, 2001, **5**, 55–64.

6 K. N. Tu, A. M. Gusak and M. Li, *J. Appl. Phys.*, 2003, **93**, 1335–1353.

7 L. M. Castano and A. B. Flatau, *Smart Mater. Struct.*, 2014, **23**, 053001.

8 (*a*) *Flexible electronics: materials and applications*, ed. W. S. Wong and A. Salleo, Springer Science & Business Media, 2009; (*b*) W. H. Qi and M. P. Wang, *Mater. Chem. Phys.*, 2004, **88**, 280–284.

9 C. D. Zou, Y. L. Gao, B. Yang, Q. J. Zhai, C. Andersson and J. Liu, *Soldering Surf. Mount Technol.*, 2009, **21**, 9–13.

10 C. D. Zou, Y. L. Gao, B. Yang, X. Z. Xia, Q. J. Zhai, C. Andersson and J. Liu, *J. Electron. Mater.*, 2009, **38**, 351–355.

11 D. C. Lin, G. X. Wang, T. S. Srivatsan, M. Al-Hajri and M. Petraroli, *Mater. Lett.*, 2003, **57**, 3193–3198.

12 K. C. Yung, C. M. T. Law, C. P. Lee, B. Cheung and T. M. Yue, *J. Electron. Mater.*, 2012, **41**, 313–321.

13 A. Roshanghias, G. Khatibi, A. Yakymovych, J. Bernardi and H. Ipser, *J. Electron. Mater.*, 2016, **45**, 4390–4399.

14 S. Pang and K. Yung, *Mater. Trans.*, 2012, **53**, 1770–1774.

15 A. Roshanghias, A. Yakymovych, J. Bernardi and H. Ipser, *Nanoscale*, 2015, **7**, 5843–5851.

16 L. Hsiao and J. Duh, *J. Electrochem. Soc.*, 2005, **152**, J105–J109.

17 C. Y. Lin, J. H. Chou, Y. G. Lee and U. S. Mohanty, *J. Alloys Compd.*, 2009, **470**, 328–331.

18 H. Jiang, K. Moon, F. Hua and C. P. Wong, *Chem. Mater.*, 2007, **19**, 4482–4485.

19 H. Zhang, J. Zhang, Q. Lan, H. Ma, K. Qu, B. Inkson, N. Mellors, D. Xue and Y. Peng, *Nanotechnology*, 2014, **25**, 425301.

20 T. T. Bao, Y. Kim, J. Lee and J. Lee, *Mater. Trans.*, 2010, **51**, 2145–2149.

21 N. Oehl, M. Knipper, J. Parisi, T. Plaggenborg and J. Kolny-Olesiak, *J. Phys. Chem. C*, 2015, **119**, 14450–14454.

22 R. Mishra, A. Zemanova, A. Kroupa, H. Flandorfer and H. Ipser, *J. Alloys Compd.*, 2012, **513**, 224–229.

23 H. Chen, Z. Li, Z. Wu and Z. Zhang, *J. Alloys Compd.*, 2005, **394**, 282–285.

24 S. Chen, C. Chen, Z. P. Luo and C. Chao, *Mater. Lett.*, 2009, **63**, 1165–1168.

25 F. Frongia, M. Pilloni, A. Scano, A. Ardu, C. Cannas, A. Musinu, G. Borzone, S. Delsante, R. Novakovic and G. Ennas, *J. Alloys Compd.*, 2015, **623**, 7–14.

26 Y. Shu, K. Rajathurai, F. Gao, Q. Cui and Z. Gu, *J. Alloys Compd.*, 2015, **626**, 391–400.

27 Y. Shu, S. Gheybi Hashemabad, T. Ando and Z. Gu, *Mater. Des.*, 2016, **111**, 631–639.

28 Y. Zhao, Z. Zhang and H. Dan, *J. Mater. Chem.*, 2004, **14**, 299–302.

29 D. C. Lin, S. Liu, T. M. Guo, G.-X. Wang, T. S. Srivatsan and M. Petraroli, *Mater. Sci. Eng., A*, 2003, **360**, 285–292.

30 K. Mohankumar and A. A. O. Tay, *EPTC 2004, Proceedings of 6th*, 2004, pp. 455–461.

31 T. Fouzder, Y. C. Chan and D. K. Chan, *J. Mater. Sci.: Mater. Electron.*, 2014, **25**, 5375–5387.

32 L. C. Tsao and S. Y. Chang, *Mater. Des.*, 2010, **31**, 990–993.

33 M. Amagai, *Microelectron. Reliab.*, 2008, **48**, 1–16.

34 A. K. Gain and L. Zhang, *J. Mater. Sci.: Mater. Electron.*, 2016, **27**, 781–794.

35 A. K. Gain and L. Zhang, *J. Mater. Sci.: Mater. Electron.*, 2015, **26**, 7039–7048.

36 A. T. Tan, A. W. Tan and F. Yusof, *Sci. Technol. Adv. Mater.*, 2015, **16**, 033505.

37 Y. Tang, G. Y. Li, D. Q. Chen and Y. C. Chen, *J. Mater. Sci.: Mater. Electron.*, 2014, **25**, 981–991.

38 J. Sopousek, J. Vrestal, A. Zemanova and J. Bursik, *J. Min. Metall., Sect. B*, 2012, **48**, 419–425.

39 A. Roshanghias, J. Vrestal, A. Yakymovych, K. W. Richter and H. Ipser, *CALPHAD*, 2015, **49**, 101–109.

40 C. E. White, *Phase Diagrams of Indium Alloys and their Engineering Applications (Monograph Series on Alloy Phase Diagrams, No. 8)*, ASM International, 1992.

41 L. Rycerz, *J. Therm. Anal. Calorim.*, 2013, **113**, 231–238.